Soft Matter

Droplet-train induced spatiotemporal swelling regimes in elastomers

Journal:	*Soft Matter*
Manuscript ID	SM-ART-05-2018-000977.R1
Article Type:	Paper
Date Submitted by the Author:	08-Jun-2018
Complete List of Authors:	Phadnis, Akshay; Arizona State University, School for Engineering of Matter, Transport and Energy Manning, Kenneth; Arizona State University, School for Engineering of Matter, Transport and Energy Sanders, Ian; Arizona State University, School for Engineering of Matter, Transport and Energy Burgin, Timothy; Joint Research and Development Inc.; Arizona State University, School of Molecular Sciences Rykaczewski, Konrad; Arizona State University, School for Engineering of Matter, Transport and Energy

Droplet-train induced spatiotemporal swelling regimes in elastomers

Akshay Phadnis[1], Kenneth C. Manning[1], Ian Sanders[1], Timothy Burgin,[2,3] and Konrad Rykaczewski[1,*]

1. School for Engineering of Matter, Transport and Energy, Arizona State University, Tempe, AZ 85287

2. Joint Research and Development Inc., 50 Tech Parkway, Stafford, VA 22556
3. School of Molecular Sciences, Arizona State University, Tempe, AZ, 85287

*corresponding author email: konradr@asu.edu

Abstract

In this work, we perform a combined experimental and numerical analysis of elastomer swelling dynamics upon impingement of a train of solvent droplets. We use time scale analysis to identify spatiotemporal regimes resulting in distinct boundary conditions that occur based on relative values of the absorption timescale and the droplet train period. We recognize that when either timescale is significantly larger than the other, two cases of quasi-uniform swelling occur. In contrast, when the two timescales are comparable, a variety of temporary geometrical features due to localized swelling are observed. We show that the swelling feature and its temporal evolution depends upon geometric scaling of polymer thickness and width relative to the droplet size. Based on this scaling, we identify six cases of localized swelling and experimentally demonstrate the swelling features for two cases representing limits of thickness and width. A finite element model of local swelling is developed and validated with experimental results for these two cases. The model is subsequently used to explore the swelling behavior in the rest of the identified cases. We show that depending upon the lateral dimension of the sample, swelling can locally exhibit mushroom, mesa, and cap like shapes. These deformations are magnified during the droplet-train impact but dissipate during post-train polymer equilibration. Our results also show that while swelling shape is a function of lateral dimensions of the sample, the extent of swelling increases with the elastomer sample thickness.

Keywords: droplet impact, polymer swelling, finite element method

Introduction

A crosslinked network of a polymer can absorb large amounts of suitable solvent and undergo elastic deformation, a phenomenon known as swelling.[1–4] Wherein, small molecules of the solvent migrate into the cross-linked network due to a difference in the chemical potential, to form a gel. Many natural materials including lentils, grains, fibers, and seeds exhibit this behavior in response to water present in their environment.[5–8] In industrial applications, solvent induced swelling of manmade polymers is used in numerous technical applications including drug delivery,[9] flow control,[10] actuation,[8,11,12] rapid containment of organic liquid spills,[13,14] and selective membrane filtration.[15,16]

Depending upon the extent of contact with the solvent, the polymer can undergo bulk swelling, where the polymer matrix is in contact with the solvent at all of its surfaces. In contrast, if only a part of the surface is in contact with the solvent, localized swelling is observed. Bulk swelling behavior in polymers has been extensively studied both experimentally[17–19] and numerically.[2,20–24] Droplet induced localized swelling has received a lot of attention recently. Recent experimental and numerical studies of droplet induced localized shape modulations and surface deformations have focused on bending and twisting of soft polymer structures,[25–29] formation of surface patterns and instabilities,[30–35] development of rapid responsive surfaces[36,37] etc. We note that due to negligible contact angle between swelling liquid and polymer, such shape modulation is distinct from elastocapillary deformations.[38–41] In addition, localized swelling of polymer structures upon impact of multiple sequential droplets (i.e. droplet train) has not yet been explored.

Repeated contact with the solvent at the same location induces swelling, deforming the polymer in an incremental fashion. The dynamics of this local swelling deformation can be compared to the formation of stalagmites due salt deposition. However, unlike stalagmites, the material expansion is restricted by the saturation of the polymer at the equilibrium. The droplet induced swelling of this kind is temporal in nature and, dependent on problem parameters, could either be highly localized or nearly uniform across the sample. Studying these swelling interactions can play an important role in designing materials for rapid and selective absorption of organic chemicals or oils droplets[14] and for designing protective gear that self-seals when exposed to droplets of harmful chemical weapon agents.[42] In this paper, we conduct a theoretical and experimental study of localized swelling behavior of polymer samples with axisymmetric geometries upon central impact of a train of solvent droplets. Based on timescale and geometric scaling analysis, we identify spatiotemporal swelling regimes with distinct, temporary geometrical deformations. We experimentally reveal a subset of these temporary deformations and use this data to validate a high fidelity numerical model that captures solvent spreading, absorption, and diffusion as well as polymer swelling. Owing to its robustness, we implemented coupled fluid permeation and large deformation theory in a finite element (FE) analysis framework to describe the swelling behavior.[20,43–47] The FE framework captures the transient and nonlinear aspects of swelling and has been previously proven to be a highly efficient numerical technique.[22,24,48–50] The validated multiphysics model is implemented to reveal characteristic deformations within the entire swelling regime map.

Swelling regimes

When a single droplet of solvent comes in contact with a polymer, droplet spreading and absorption into the bulk polymer occur and induce swelling at and below the contact interface. In this event, the two relevant time scales are the liquid spreading time, t_s, and the time required for absorption of the droplet into bulk of the polymer, t_a. For surfaces that are wetted by the impacting droplet, t_s scales with R_d and is in most cases much shorter than $t_a \sim R_d^2/D$ (where R_d is droplet radius and D is the solvent diffusion coefficient in the polymer).[51] For example, for hexane droplet with $R_d =$ 1.3 mm impacting on a Polydimethylsiloxane (PDMS) surface, $t_s =$ 18-20 ms while $t_a =$ 12-15 s. When a train of droplets impinges on the polymer surface (see Fig. 1(a)), another time scale set by the time-period between two droplets, t_{dt} (referred from now on as droplet train period), emerges. In case t_s is comparable to t_a (e.g. for impact of extremely viscous liquids), the summation of these parameters is the appropriate droplet train impact time scale. However, since in most cases absorption, not spreading, is the rate limiting process, we utilize t_a and t_{dt} as the two relevant time scales for analysis of the droplet-train and polymer sample dynamics. Depending upon the relative magnitudes of these times scales, three different regimes illustrated in Fig. 1(a) arise:

- $t_a \gg t_{dt}$: In this case the droplet impacts the surface before the preceding droplet is completely absorbed. The progression of impacting droplets leads to flooding of the contact surface and eventually of the rest of polymer sample. While during the sample flooding time some deformation of the polymer occurs, this case can be approximated by a scenario where a sample is submerged in the solvent bath and allowed to swell freely. This case has been studied in detail and is described in the literature.[21,24,45,48]
- $t_a \ll t_{dt}$: In this case each droplet is completely absorbed and the polymer may reach an equilibrium swelling condition before the next droplet hits. Thus, a train of droplets in this case leads to a quantized growth mode, with final state of each step corresponding to temporary equilibrium (i.e. uniform polymer stretching in all the unconstrained directions). Volumetric constraint is used to estimate the swelling ratio of the polymer, given the concentration of the solvent.[45] The incremental swelling ratio defined as the ratio of final to

initial (dry) volume of the polymer due to absorption of n droplets in time nt_{dt} can be obtained by rewriting the volumetric constraint as

$$J_n = 1 + \Omega n c_d$$

where, c_d is the molar concentration when a single droplet is absorbed, n is the number of droplets. This swelling ratio can be further expressed in terms of the droplet parameters by rewriting the concentration c_d as

$$J_n = 1 + \frac{\Omega n V_d \rho}{M_w V_P} = 1 + \frac{n V_d}{V_p}$$

where, V_d is the volume of the droplet, V_p is the initial volume of the polymer, M_w, ρ, and Ω is the molecular weight, density, and molar volume of the solvent, respectively.

- $t_a \sim t_{dt}$: In this case, the time in-between droplet impact is comparable to liquid absorption time into the bulk polymer and it is difficult to predict polymer swelling dynamics based on timescale analysis alone. Consequently, we focus our attention on studying the localized swelling behaviors possible in this regime.

Pertaining to the third regime, we now consider effects of the possible variations of the polymer sample width and thickness relative to the droplet radius. We focus on a situation where the successive droplets impact the surface as soon as the previous one is absorbed into the bulk polymer. We consider an axisymmetric problem formulation, where a sessile droplet of radius R_d, is deposited on the center of upper planar surface of a cylinder with thickness δ and lateral dimension, L. Based on these three dimensions, the following six scenarios illustrated in Fig. 1(b) are possible: (i) $R_d \gg \delta$ and $R_d \sim L$, (ii) $R_d \sim \delta$ and $R_d \sim L$, (iii) $R_d \ll \delta$ and $R_d \sim L$, (iv) $R_d \gg \delta$ and $R_d \ll L$, (v) $R_d \sim \delta$ and $R_d \ll L$, and (vi) $R_d \ll \delta$ and $R_d \ll L$. We note that all cases in which $R_d \gg L$ are trivial as the solvent will flood the entire polymer and are analogous to the

$t_a \gg t_{dt}$ regime. Similarly, in cases (i) and (ii) volume of the polymer sample and the droplet are comparable, consequently impact of droplet train will result in sample flooding and bath-like swelling behavior, ending in polymer saturation after impact of a few droplets (depending on swelling capability of the solid). In the remainder of the cases (iii-vi), however, localized swelling with distinct geometrical deformations can occur.

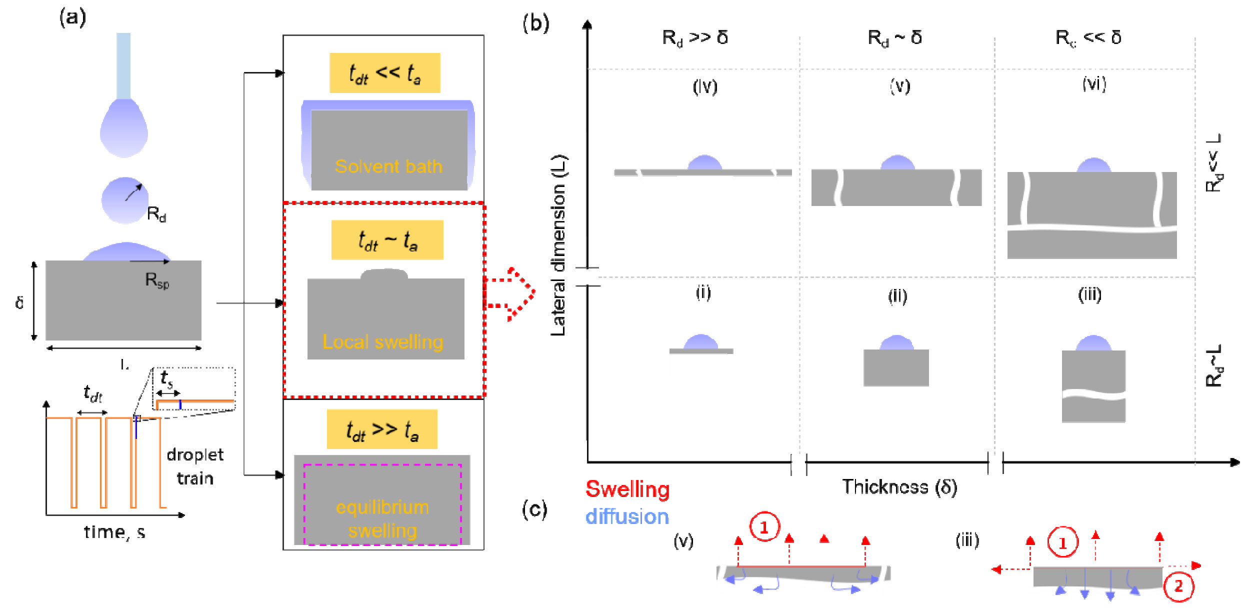

Fig. 1 Regime map based on interactions between droplet and polymer surface: (a) regimes due to relation between the time scales associated with diffusion and train of droplets, (b) regime map based on geometric possibilities of the droplet and polymer surface for the case where the two time scales are comparable, and (c) close-up view of the expected near surface swelling and diffusion mechanisms in cases (iii) and (v).

In case (iii), diffusion of the solvent will occur predominantly along the thickness of the sample (i.e. negligible in-plane concentration gradients) and we expect swelling to occur in both transverse and lateral direction (see Fig. 1(c)-iii). In cases (iv) and (v), solvent will rapidly saturate volume below the droplet and its diffusion will gradually occur along the lateral dimension of the sample (see Fig. 1(c)-v). Consequently, swelling will occur predominantly in the transverse direction below the liquid-surface contact region. In turn, case (vi) corresponds to a semi-infinite sample with isotropic solvent fluxes. We expect swelling in this case to be qualitatively similar to case (v), but with significant decrease in the extend of the local sample deformation. In case (iv) microscopic crumpling and buckling of the thin polymer film ($\delta < 100$ μm) occurs, irrelevant of the swelling induced by exposure to solvent drops or bath (see representative experiments in ESI). Thin film buckling has been studied extensively in literature,[30–32] and we will not elaborate on it further.

Based on the above qualitative arguments, we expect the most distinct and substantial local deformations to occur in cases (iii) and (v). Consequently, these two scenarios provide the best study cases for high temporal and spatial resolution experimental characterization of the droplet-train induced polymer swelling dynamics. In the following sections, we describe results of these experimental efforts and use them to validate the multiphysics FE model developed to simulate the swelling dynamics. The numerical model validated against experimental results from cases (iii) and (v) is subsequently used to study swelling characteristics in rest of the cases that were identified using scaling analysis.

Results and discussion

In this section we describe the experimental and numerical studies of localized swelling dynamics in cases (iii) and (v) represented by central impact of n-hexane droplet-train on PDMS cylinder and disc, respectively. We selected this representative polymer-solvent pair because of the high degree of swelling[52] and availability of values of parameter required for modeling. We imaged the sample swelling dynamics using a custom-built droplet dispenser setup with a backlight and camera schematically illustrated in Fig. 2(a). We also developed an axisymmetric FE model of the process (see schematic formulation in Fig. 2(b)) and compared it against the experimental data. Further experimental and numerical details are described in the Methods Section.

A key link between the experimental and numerical efforts, is the determination of the value of the diffusion coefficient of the solvent within the polymer. In particular, an accurate value of this parameter is needed in order to simulate correctly the temporal polymer shape evolutions due to droplet train swelling. Since very limited data was available in literature, we conducted two sets of experiments to measure the diffusion coefficient of n-hexane in PDMS cured with 1:33 cross-linker to base ratio. The results of these experiments are described first, followed by discussion of the cylinder and disc swelling studies, and numerical exploration of swelling dynamics in the remaining cases.

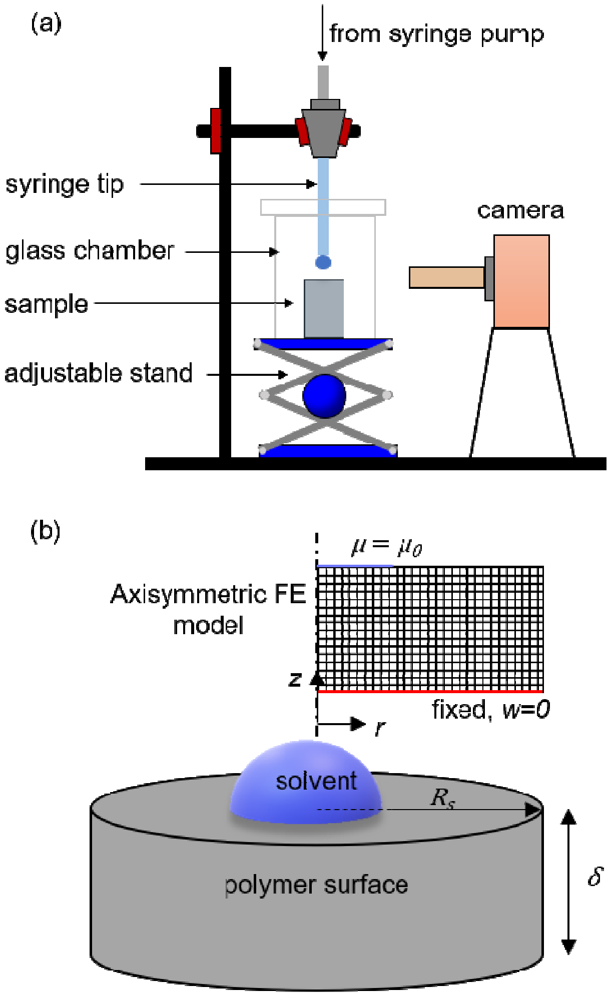

Fig. 2 (a) Schematic of the experimental setup used to observe PDMS cylinder and disc swelling dynamics upon impact of n-hexane droplet train and (b) schematic formulation of the corresponding two dimensional axisymmetric FE model domain and boundary conditions.

Measurement of hexane diffusion coefficient in PDMS

To determine the diffusion coefficient of n-hexane in PDMS cured with 1:33 cross-linker to base ratio, we conducted polymer free swelling experiments in solvent bath and Attenuated Total Reflectance Fourier Transform Infrared Spectroscopy (ATR-FTIR). In the free swelling experiments, we measured the mass of n-hexane absorbed by the PDMS sample with time (see ESI for further details). In the ATR-FTIR experiments, we measured the temporal change in spectral reflectance at the ATR crystal-polymer interface after top of the sample was exposed to the solvent. The diffusion coefficient can be determined from the onset time for reflectance change and the subsequent spectral dip evolution.[53–55] Since in our experiments swelling of the polymer film changed its thickness during the experiments, we could not apply traditional closed-form formulas to determine the diffusion coefficient. Instead, we estimated D through iteratively adjusting its value in the FE simulations (adopted for geometries in these experiments) and comparing against experimental values. Using this approach, we found that $D = 6.1\times10^{-9}$ m^2s^{-1} provided best match of the simulated shape with free swelling data. This value is within the 2.6×10^{-9} to 7.0×10^{-9} m^2s^{-1} (95% confidence interval) range obtain from the ATR-FTIR experiments and is also in decent agreement with 4.0×10^{-9} m^2s^{-1} value previously reported in the literature (albeit for PDMS cured with 1:10 cross-linker to base ratio).[56] Consequently, in the subsequent studies we used $D = 6.1\times10^{-9}$ m^2s^{-1} as well as the lower and upper bounds of the 95% confidence interval from ATR-FTIR experiments.

Localized swelling of cylindrical sample (case iii)

As a representative scenario for case (iii), we studied central impact of 34 n-hexane droplets within a 10 minute period onto a cylindrical sample of PDMS with radius $R_s = 5$ mm and thickness $\delta = 12.5$ mm. After contact, each droplet with volume of around 10 μL (pre-impact radius of around 1.3 mm) spreads within 18 to 20 ms and forms a puddle with radius of about 5 mm. Thus, the geometrical conditions for case (iii) of $R_d \ll \delta$ and $R_d \sim L = 2R_s$ are satisfied. In order to satisfy the temporal regime requirement of matching t_a and t_{dt}, we adjusted solvent flow rate so that droplets impinged on the surfaces every 12 to 15 s. This period corresponds to the experimentally measured time taken by the sample to completely absorb the sessile liquid puddle from each of the first few individual droplets (see ESI).

Representative sequential profile images of the cylinder swelling dynamics are shown in Fig. 3(a) and Movie 1. In agreement with our previous reasoning, the comparable size of the cylinder and the droplet puddle results in substantial swelling in both radial and axial directions. This process creates a spherical cap in the center of the sample, while the sides of the cylinder swell outwards radially, creating a profile resembling a "mushroom". During impact of the first few droplets the deformation of the top surface is slightly asymmetrical. This behavior eventually disappears as subsequent droplets spread out more evenly, resulting in symmetrical deformation after 10 minutes of the experiment.

The upper possible bound of the local deformation in the axial direction is defined by the equilibrium stretching ratio, λ_{eq}, which can be expressed in terms of the swelling ratio defined as $\lambda_{eq} = \sqrt[3]{J_{eq}} = \sqrt[3]{V_{swollen}/V_{dry}}$. From our free swelling experiments, we obtained $J_{eq} = 2.71$ and

$\lambda_{eq} = 1.39$. Since we used PDMS base to cross-linker to ratio of 33:1, our value of $J_{eq} = 2.71$ is higher than previously reported value of 1.35 that were measured for base to cross-linker ratio of 10:1.[52] For the center of the cylinder, we observed the maximum equilibrium stretching ratio of 1.1. This value is smaller than λ_{eq} because the sample is only locally saturated.

The bottom sequence of profile images of the simulated cylinder swelling dynamics shown in Fig. 3(a) illustrate good agreement with experimental results. In more quantitative terms, the plots in Fig. 3(b) show a close match between extracted profile of the cylinder obtained from experiments and simulations after 2, 5, 7, and 10 minutes of the impact of the first droplet. The FE model was setup to simulate the test conditions by defining droplet contact boundary on the entire top surface of the cylinder as shown in Fig. 2(b). The pulsating nature of droplet contact on the top boundary was simplified by assuming constant contact with the solvent. This simplification matches with the studied scenario where a droplet meets the surface as soon as the previous one is absorbed. The only inputs into the model are the shear modulus (75 kPa for a PDMS mixed in 33:1 ratio),[57] Flory's interaction parameter ($\chi = 0.4$),[58] and experimentally measured diffusion coefficient of n-hexane in the polymer. The range of the presented simulation results corresponds to the diffusion coefficient range that we measured. The dark line in plots in Fig. 3(b) corresponds to $D = 6.1\times10^{-9}$ m^{2}s^{-1} obtained in the free swelling experiments, while the cyan band corresponds to the 2.6×10^{-9} to 7.0×10^{-9} m^{2}s^{-1} result range (95% confidence interval) obtained from the ATR-FTIR experiments. As more droplets hit the substrate and swelling proceeds, the deformation profiles simulated with $D = 6.1\times10^{-9}$ and $D = 7.0\times10^{-9}$ m^{2}s^{-1} come closer and begin to overlap. After 10 minutes, surface of the cylinder gets saturated and reaches and equilibrium state, locally. Similar phenomenon is also observed for the swelling of thin film which is discussed next.

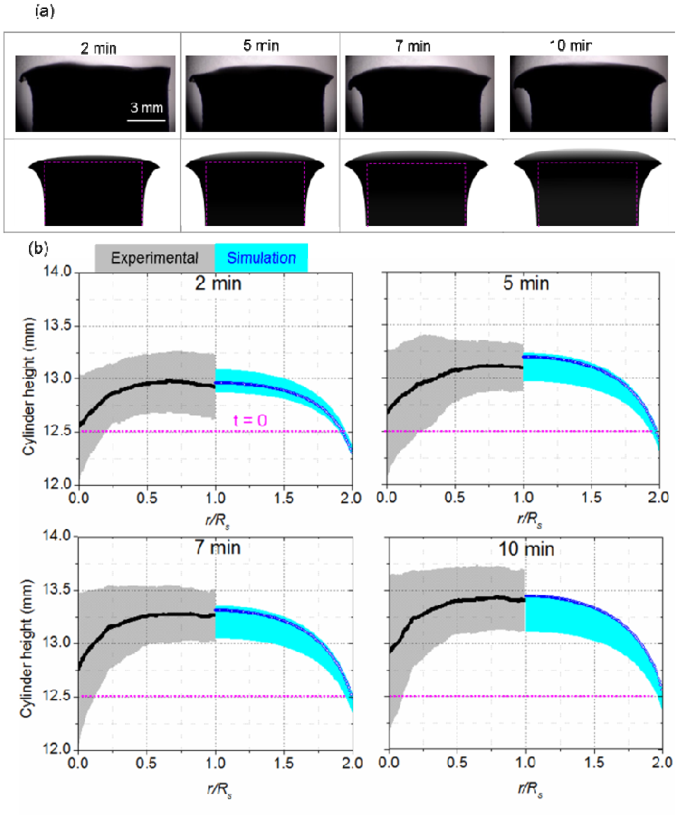

Fig. 3 Characteristic swelling of cylindrical samples: (a) sequence of experimental (top row) and simulated (bottom row) cylinder deformation profiles at corresponding time points, and (b) comparison between experimental (left) and numerical results (right) showing temporal evolution of the top surface after 2, 5, 7, and 10 minutes. Error band for experimental results correspond to 68% confidence interval of the experimental measurements, while the error band for numerical results stems from the variation in the measured diffusion coefficient implemented in the numerical simulations.

Localized swelling of the disc sample (case v)

As a representative geometry for case (v), we studied central impact of 28 n-hexane droplets within a 7 minute period onto a disc of PDMS with radius R_s =12.5 mm and thickness $\delta =$ 1 mm. In order to satisfy the geometric and temporal regime requirements, droplet size and solvent flow rate were maintained the same as in case (iii) experiments. Specifically, these parameters allowed for satisfaction of the geometrical conditions of $R_d \sim \delta$ and $R_d \ll L = 2R_s$ as well as the temporal regime condition of matching t_a and t_{dt}.

Representative sequential profile images of dynamic swelling of the disc is shown in Fig. 4(a) and Movie 2. In agreement with our previous reasoning, the deformation has a “mesa” like shape that is highly localized to the region below droplet-surface contact and rapidly decays away from the edge of this area. The “mesa” height increases with time until polymer saturation is achieved after about 7 minutes of the experiment start. As shown by the bottom sequence of profile images of the simulated disc swelling dynamics in Fig. 4(a), our numerical results match well with our experimental observations. The maximum λ_{eq} is 1.5$\pm$0.1 which is close to the equilibrium stretching ratio of 1.4 obtained from free swelling test. This agreement stems from local saturation of the sample throughout its thickness, which did not occur in case (iii). We note that the absorption of initial few droplets leads to temporary mechanical instabilities of the surface and its crumpling. This, in turn, results in shedding of a few droplets. Since these effects were not captured in the model formulation, we used a time averaged area to define the solvent contact with the polymer surface in order to accommodate the droplet shedding process. Using this area, the sample within the model imbibed nearly all of the experimentally dispensed solvent volume (97%) in 7 minutes. This minor alteration of the numerical boundary conditions results in small overestimation of the deformation in the early swelling stage (see frame of Fig. 4(b) corresponding to results at 1 minute). Besides this minor disagreement, our simulations provide a good prediction of the swelling dynamics of cylindrical and disc polymer samples subjected to impact of a solvent droplet train.

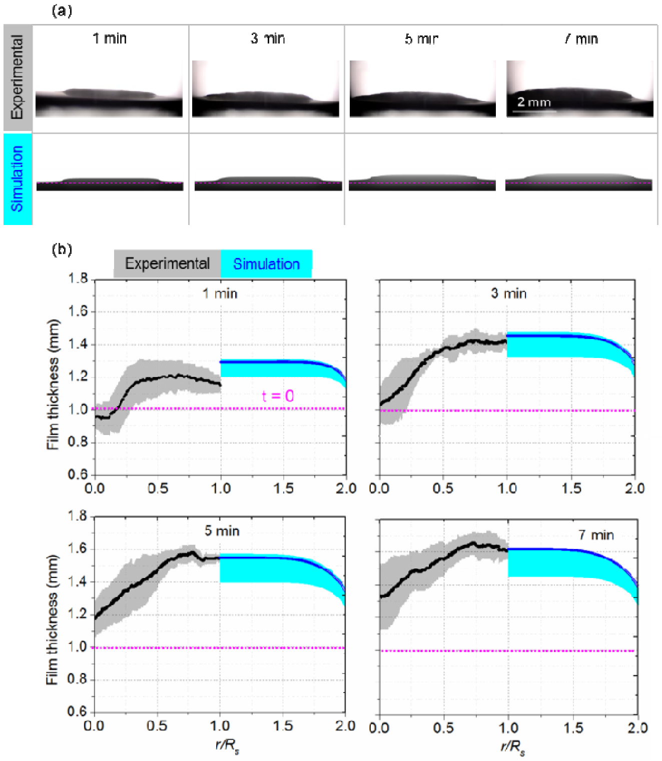

Fig. 4 Characteristic swelling of film samples: (a) sequence of experimental (top row) and simulated (bottom row) disc deformation profiles at corresponding time points and (b) comparison between experimental (left) and numerical results (right) showing temporal evolution of the surface at 1, 3, 5, and 7 minutes of the experiment. Error band for experimental results correspond to 68% confidence interval of the experimental measurements, while the error band for numerical results stems from the variation in the measured diffusion coefficient implemented in the numerical simulations.

Localized swelling deformations in the matched timescale regime

Using the validated numerical model, we simulated n-hexane droplet-train induced swelling of the PDMS with geometries corresponding to the cases (ii) to (vi) discussed in the swelling regime section (see Fig. 1(c)). The simulated swelling deformations resulting from impact of 30 droplets are summarized in Fig. 5(a). We note that in case (ii) we set the sample thickness to 4 mm instead of 1 mm as in case (v) in order to allow for the absorption of all of the 30 droplets (geometrical regime requirements are still satisfied since $\delta/R_d \approx 4 < 10$). Overall, we categorize the geometric form of the deformation into three characteristic shapes *viz.*, the "mushroom" for case (ii) and (iii), the "mesa" for cases (iv) and (v), and finally the "cap" for case (vi). The subtle difference between the "cap" and the "mesa" geometries can be realized by the curvature of the swollen front at the axis of symmetry. In case (iv), the deformation is flat for most part of the swollen region whereas in case (vi), the swollen region is curvilinear. Rapid local saturation of thin film results into deformation approaching uniform local swelling, while thick sample does not saturate and has strong concentration gradients in the sample. Similar behavior is observed with case (ii) to some extent where swollen region near the center is flat as opposed to case (vi). In all, the lateral extent of the sample relative to the droplet diameter plays the dominant role in determining the localized swelling geometry ("mushroom" vs. "mesa" and "cap") and thickness dominates the further distinction between formation of "mesa" vs. "cap" shapes.

We found that localized swelling deformations can also be distinguished based on the temporal evolution of the maximum displacement that occurs at the center of the droplet-surface contact region. The data in the plot in Fig. 5(b) is presented in terms of non-dimensional time t^* that is obtained by scaling the time with the total absorption time for each case. Case (iii) shows maximum swelling displacement of about 1 mm while case (iv) shows the lowest swelling displacement of 0.18 mm. The latter case results in the lowest swelling because the sample is very thin compared to the droplet and saturates throughout its thickness rapidly. While being significantly higher than in case (iv), the maximum displacement in cases (v) and (vi) follow a similar saturation trend as case (iv). In contrast, the maximum displacement in cases (ii) and (iii) does not saturate. Consequently, the "mushroom" (cases (ii) and (iii)) shapes can also be distinguished from the "cap" and "mesa" geometries based on the temporal evolution of their maximum displacement.

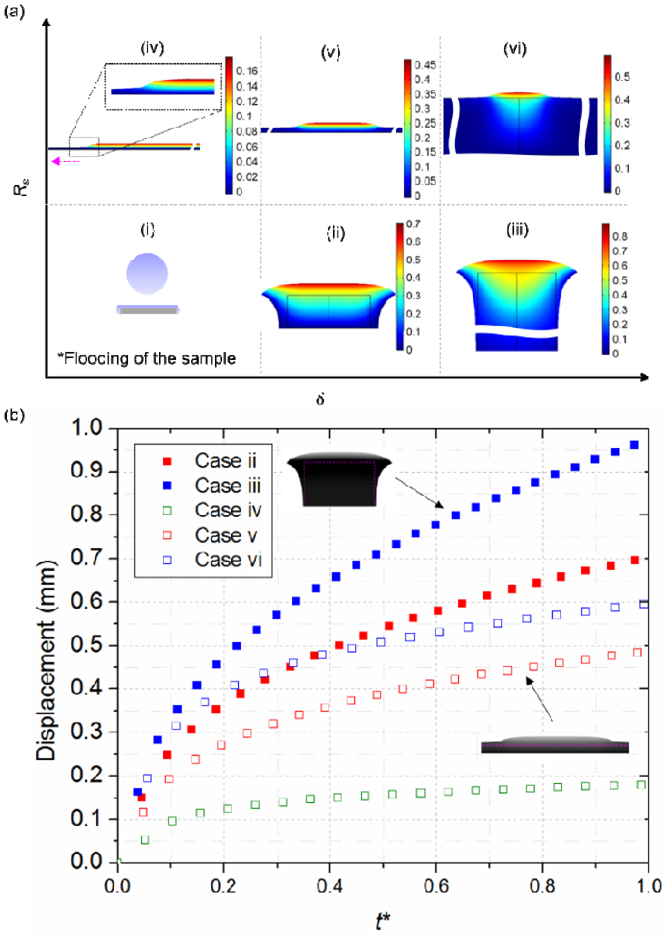

Fig. 5 (a) Characteristic swelling deformations simulated using FE model for the identified geometric regimes and (b) plot of maximum surface swelling displacement in the axial direction against non-dimensional time for all the simulated geometries.

Conclusions

We performed a combined experimental and theoretical study of localized polymer swelling dynamics under impingement of a solvent droplet train. We identified three swelling regimes based on relative comparison of the droplet train period and absorption time. When these two time scales are significantly different, swelling resembles either free swelling in a bath of solvent ($t_a \gg t_{dt}$) or quantized uniform growth with each step corresponding to a temporary equilibrium ($t_a \ll t_{dt}$). When these two time scales are comparable, appreciable localized deformation can occur near the impact of the droplets. In this regime, we identified six deformation scenarios that can occur based on the relative comparison between the droplet size and sample dimensions. We experimentally and numerically studied two of these cases in depth. Specifically, we studied localized swelling induced by central impact of about 30 droplets of n-hexane onto PDMS cylinder and disc (cases (iii) and (v)). We developed a complementary finite element model of the process and validated it against the experimental results in terms of transient swelling deformation. Using only the diffusion coefficient as the fitted parameter, we obtained good agreement between numerical and experimental results. Using the validated model, we simulated the localized swelling behavior for all the geometrical cases identified in the match absorption time and droplet impact period regime. Our results show that when the droplet size is comparable to the lateral size of the polymer sample, droplet train induced swelling results in formation of a temporary “mushroom” shape. In turn, when sample is much wider than the droplet size, droplet train induced swelling results in formation of temporary “mesa” and “cap” shapes. Our results provide a starting point for analysis of droplet train swelling induced of more complex samples and development of functional devices based on such materials.

Materials and Methods

Numerical modeling

A custom finite element swelling model is developed in COMSOL Multiphysics v5.3. A concurrent fluid permeation and large deformation theory[45] combined with constitutive relation based on Flory-Rehner theory is considered here. Following Lucantonio *et al.*[24] and Caccavo and Lamberti,[49] we cast the following governing equations in the weak form using the weak form PDE module in COMSOL. For computational simplicity, we considered a 2D axisymmetric domain. It should be noted that the lateral dimension L of polymer will henceforth be expressed as R_s, the radius of the polymer sample in a 2D axisymmetric domain. A coupled system of equations governing diffusion, mechanical deformation, and volumetric constraint are solved simultaneously to obtain solution for displacement field $u(X,t)$, concentration field $c(X,t)$ and pressure field $p(X,t)$. A volumetric constraint is imposed to account for the fact that the total volume of the swollen matrix is the sum of dry polymer volume and the volume of solvent absorbed. Finally, a finite element problem can be formulated as follows: find u, p, c and boundary concentration c_b such that for any $\hat{u}$, $\hat{c}$, $\hat{p}$ and $\hat{c_b}$ with $\hat{u}$ compatible with the boundary condition on bottom surface where $w = 0$, and $c = c_b$ on droplet contact area, it holds:

$$-2\pi \int (\boldsymbol{S}:\nabla \hat{u}) R \, dA = 0 \tag{1}$$

$$-2\pi \int \frac{\partial c}{\partial t} \, \hat{c} \, R \, dA + 2\pi \int \boldsymbol{h} \, \hat{c} \, R \, dA = 0 \tag{2}$$

$$-2\pi \int [J - (1 + \Omega \, c)] \hat{p} \, R \, dA = 0 \tag{3}$$

with a modified Dirichlet boundary condition defined in terms of boundary concentration c_b such that the chemical potential balance is satisfied on the boundary. Please note that the terms in bold are rank-2 tensors.

$$-2\pi \int (\mu_0 - \mu)\widehat{c_b} R \, dL = 0 \qquad (4)$$

where, 1st Piola-Kirchhoff stress ***S***, chemical potential μ and solvent flux ***h*** is defined as-

$$\boldsymbol{S} = \frac{G}{\lambda_0} \boldsymbol{F_0} \boldsymbol{F_0^T} \boldsymbol{F} - p \; J \; \boldsymbol{F^{-T}} \qquad (5a)$$

$$\mu = RT \left(\log \left(\frac{\Omega J_0 c}{1 + \Omega J_0 c} \right) + \frac{1}{1 + \Omega J_0 c} + \frac{\chi}{(1 + \Omega J_0 c)^2} \right) + \Omega p \qquad (5b)$$

$$\boldsymbol{h} = -\frac{c(X,t) D}{RT} \; \boldsymbol{F^{-T}} \boldsymbol{F^{-1}} \nabla \mu \qquad (5c)$$

where, $\boldsymbol{F}$ is the deformation gradient, G is shear modulus of the dry polymer (kPa), p is Lagrange multiplier and is equivalent to an osmotic pressure (Pa), Ω is molar volume (m^3 mol^{-1}), χ is the interaction parameter, $J = \det \boldsymbol{F}$ is the volumetric swelling ratio and D is the diffusion coefficient of the solvent in the dry polymer (m^{2}s^{-1}). Since the chemical potential reaches singularity at $c = 0$, a reference state is assumed where infinitesimal swelling ratio $J_0 = 1.003$ and concentration $c_0 = 23 \, mol/m^3$ is defined in the numerical model. Naturally, all the calculations that follow, use this reference state as the initial condition instead of a dry state.[24]

A schematic of polymer droplet interaction and corresponding 2D axisymmetric FE model domain is shown in Fig.2. The droplet-surface contact area after the droplet has completely spread, is defined with the modified Dirichlet condition as explained earlier, while the rest of the boundary is defined with zero solvent flux, i.e., insulated. The bottom surface is constrained for any motion in axial direction ($w = 0$).

Polymer sample preparation

PDMS was prepared by mixing Sylgard 184 (Dow Corning) base with cross-linker in 33:1 ratio by mass. Red dye was added (KEDA dye) to facilitate visual distinction of the sample from the impacting solvent. The mixture was cast into cylindrical Aluminum molds and cured at 60 ˚C for 1 hour. Using same mixing procedure, uncured PDMS was coated on the glass slides of size 25 × 25 mm. As a result, uniform films of PDMS having thickness 0.9±0.1 mm were obtained.

Experimental Setup

Solvent droplets were produced using a stainless steel dispenser tip with internal diameter of 0.5 mm. In order to facilitate dispensing of smaller drops, the tip surface was made hydrophobic with a treatment of a mixture of Nitic acid (Sigma-Aldrich), water and ethanol (200 proof, Sigma Aldrich), and 1H,1H,2H,2H-Perfluorodecyl-triethoxysilane (Gelest). The steel dispenser tips were dipped in the solution for 1 hour and dried using a heat gun. This treatment reduced the extent to which hexane wetted the tip and made production of consistent sized droplets easier. The dispenser tip was connected to a 3 mL-syringe fitted onto a syringe pump (NE-300, New Era Pump Systems, Inc.) using a PTFE chemical resistant tubing and Luerlok connectors. To isolate the droplets from the effect of air movement inside the fume hood, the sample and the tip were situated inside a square glass container closed with a lid. This arrangement reduced the drift coming into the fume hood and ensured constant droplet frequency. To reduce the droplet evaporation, the sample was placed over a pool of hexane to create saturated vapor space. The evaporation time in this situation for a 10 μL droplet was measured to be > 2 min which is significantly higher than the absorption time (~ 12−15 sec) and hence the droplet evaporation was neglected. In order to prevent complex spreading dynamics, droplets were released from height of 5 mm above the sample, which resulted in small Weber number of 4 to 10 and negligibly small inertia effects.

Imaging

Nikon D5200 DSLR camera attached with an optical lens (489052, Navitar) was used for imaging the droplet impact. A monochromatic light source (Sola Eng, Litepanels) was used to backlight the setup. The images were post processed using MATLAB code based on Otsu's algorithm.[59] Please refer to Fig.S3 in ESI for further details of the experimental setup.

Acknowledgement

The authors would like to thank Naval Engineering Education Consortium grant number N00174-15-0001 administered by Naval Surface Warfare Center Dahlgren Division for the financial support. We thank Dr. Liping Wang and Ms. Xiaoyan Ying from ASU for their help in conducting ATR-FTIR experiments. Authors would also like to thank Mr. Praveen Kotagama and Ms. Namrata Kanth for the overall suggestions and comments on the manuscript.

References

1 D. J. Buckley, M. Berger and D. Poller, *J. Polym. Sci.*, 1962, **56**, 163–174.

2 M. Doi, *J. Phys. Soc. Japan*, 2009, **78**, 52001.

3 D. J. Tanaka and T. Fillmore, *J.Chem. Phys.*, 1979, **70**, 1214-1218.

4 M. Daoud, E. Bouchaud and G. Jannink, *Macromolecules*, 1986, **19**, 1955–1960.

5 E. Reyssat and L. Mahadevan, *J. R. Soc. Interface*, 2009, **6**, 951-957.

6 B. P. N. Singh and S. P. Kulshrestha, *J. Food Sci.*, 1987, **52**, 1538–1541.

7 M. J. Harrington, K. Razghandi, F. Ditsch, L. Guiducci, M. Rueggeberg, J. W. C. Dunlop, P. Fratzl, C. Neinhuis and I. Burgert, *Nat. Commun.*, 2011, **2**, 337.

8 P. Fratzl and F. G. Barth, *Nature*, 2009, **462**, 442–448.

9 Y. Qiu and K. Park, *Adv. Drug Deliv. Rev.*, 2001, **53**, 321–339.

10 D. T. Eddington and D. J. Beebe, *Adv. Drug Deliv. Rev.*, 2004, **56**, 199–210.

11 S. Ahn, R. M. Kasi, S. C. Kim, N. Sharma and Y. Zhou, *Soft Matter*, 2008, **4**, 1151-1157.

12 Z. Liu and P. Calvert, *Adv. Mater.*, 2000, **12**, 288–291.

13 T. Ono, T. Sugimoto, S. Shinkai and K. Sada, *Nat. Mater.*, 2007, **6**, 429–433.

14 J. B. Fan, Y. Song, S. Wang, J. Meng, G. Yang, X. Guo, L. Feng and L. Jiang, *Adv. Funct. Mater.*, 2015, **25**, 5368–5375.

15 W. A. Akber Hassan and X. Jiang, *Greenh. Gases Sci. Technol.*, 2012, **2**, 408–418.

16 M. S. Mittenthal, B. S. Flowers, J. E. Bara, J. W. Whitley, S. K. Spear, J. D. Roveda, D. A. Wallace, M. S. Shannon, R. Holler, R. Martens and D. T. Daly, *Ind. Eng. Chem. Res.*, 2017, **56**, 5055–5069.

17 E. C. Achilleos, R. K. Prud'homme, I. G. Kevrekidis, K. N. Christodoulou and K. R. Gee, *Aiche J.*, 2000, **46**, 2128–2139.

18 S. Sotoudeh, G. Pourfallah, A. Barati, R. Davarnejad, M. A. Farahani and A. Memar, *Ind. Eng. Chem. Res.*, 2010, **49**, 10111–10115.

19 O. Uz Okay and S. B. Sariisik, *Eur. Polym. J.*, 2000, **36**, 393–399.

20 F. A. Escobedo and J. J. de Pablo, *Phys. Rep.*, 1999, **318**, 85–112.

21 S. A. Chester, C. V. Di Leo and L. Anand, *Int. J. Solids Struct.*, 2015, **52**, 1–18.

22 W. Hong, Z. Liu and Z. Suo, *Int. J. Solids Struct.*, 2009, **46**, 3282–3289.

23 Z. Duan, J. Zhang, Y. An and H. Jiang, 2013, **80**, 3–7.

24 A. Lucantonio, P. Nardinocchi and L. Teresi, *J. Mech. Phys. Solids*, 2013, **61**, 205–218.

25 D. P. Holmes, M. Roché, T. Sinha and H. A. Stone, *Soft Matter*, 2011, **7**, 5188.

26 M. Pezzulla, G. P. Smith, P. Nardinocchi and D. P. Holmes, *Soft Matter*, 2015, **12**, 4435–4442.

27 A. Lucantonio, P. Nardinocchi and M. Pezzulla, *Proc. R. Soc. A Math. Phys. Eng. Sci.*, 2014, **470**, 20140467.

28 L. Ionov, *Adv. Funct. Mater.*, 2013, **23**, 4555–4570.

29 D. P. Holmes, P. T. Brun, A. Pandey and S. Protière, *Soft Matter*, 2016, **12**, 4886–4890.

30 H. S. Kim and A. J. Crosby, *Adv. Mater.*, 2011, **23**, 4188–4192.

31 D. P. Holmes, M. Ursiny and A. J. Crosby, *Soft Matter*, 2008, **4**, 82–85.

32 H. Lee, J. Zhang, H. Jiang and N. X. Fang, *Phys. Rev. Lett.*, 2012, **108**, 1–5.

33 M. Guvendiren, S. Yang and J. A. Burdick, *Adv. Funct. Mater.*, 2009, **19**, 3038–3045.

34 M. Guvendiren, J. A. Burdick and S. Yang, *Soft Matter*, 2010, **6**, 5795.

35 D. P. Holmes and A. J. Crosby, *Phys. Rev. Lett.*, 2010, **105**, 1–4.

36 D. P. Holmes and A. J. Crosby, *Adv. Mater.*, 2007, **19**, 3589–3593.

37 H. Lee, C. Xia and N. X. Fang, *Soft Matter*, 2010, **6**, 4342-4345.

38 J. Liu, J. Sun and Y. Mei, *J. Appl. Phys.*, 2013, **114**, 44901.

39 J. L. Liu and X. Q. Feng, *Acta Mech. Sin.*, 2012, **28**, 928–940.

40 R. W. Style, A. Jagota, C. Y. Hui and E. R. Dufresne, *Annu. Rev. Condens. Matter Phys.*, 2016, **8**, 99–118.

41 L. Chen, E. Bonaccurso, T. Gambaryan-Roisman, V. Starov, N. Koursari and Y. Zhao, *Curr. Opin. Colloid Interface Sci.*, 2018, **36**, 46-57.

42 K. Rykaczewski, T. Burgin, *US Pat.*, 20170321373A1, 2017.

43 C. J. Durning and K. N. Morman, *J. Chem. Phys.*, 1993, **98**, 4275–4293.

44 N. R. Kenkare, C. K. Hall and S. A. Khan, *J. Chem. Phys.*, 2000, **113**, 404–418.

45 W. Hong, X. Zhao, J. Zhou and Z. Suo, *J. Mech. Phys. Solids*, 2008, **56**, 1779–1793.

46 X. Wang and W. Hong, *Proc. R. Soc. A Math. Phys. Eng. Sci.*, 2012, **468**, 3824–3841.

47 S. A. Chester and L. Anand, *J. Mech. Phys. Solids*, 2010, **58**, 1879–1906.

48 J. Zhang, X. Zhao, Z. Suo and H. Jiang, *J. Appl. Phys.*, 2009, **105**, 093522.

49 D. Caccavo and G. Lamberti, *Mater. Sci. Eng. C*, 2017, **76**, 102–113.

50 N. Bouklas, C. M. Landis and R. Huang, *J. Mech. Phys. Solids*, 2015, **79**, 21–43.

51 M. J. De Ruijter, J. De Coninck and G. Oshanin, *Langmuir*, 1999, **15**, 2209-2216.

52 J. N. Lee, C. Park and G. M. Whitesides, *Anal. Chem.*, 2003, **75**, 6544–6554.

53 X. Sun, S. Turnage, E. B. Iezzi, Y. Yang, B. Chang, N. C. Muthegowda, S. K. Balijepalli,

N. Dhuyvetter, L. P. Wang, K. N. Solanki and K. Rykaczewski, *J. Coat. Technol. Res.*, 2017, **14**, 1247–1258.

54 T. Nguyen, D. Bentz and E. Byrd, *J. Coatings Technol.*, 1995, **67**, 37–46.

55 I. Linossier, F. Gaillard, M. Romand and J. Feller, *J. Appl. Polym. Sci.*, 1997, **66**, 2465–2473.

56 M. A. Awan and J. H. Dymond, *Int. J. Thermophys.*, 2001, **22**, 679–700.

57 L. Chen, G. K. Auernhammer and E. Bonaccurso, *Soft Matter*, 2011, **7**, 9084.

58 R. A. Orwoll and P. A. Arnold, *Phys. Prop. Polym. Handb.*, 2007, **50**, 451.

59 N. Otsu, *IEEE Trans. Syst. Man. Cybern.*, 1979, **20**, 62–66.

Graphical Abstract: